

# Design, Fabrication and Testing of a Flapping-Wing Mechanism for Bio-Inspired Micro Air Vehicles

*Patrick Liotti<sup>1</sup>, Oluwatobi Adekeye<sup>2</sup>, Fidel Khouli<sup>3</sup>, Jeremy Laliberte<sup>4</sup>, Jeff Dawson<sup>5</sup>  
Carleton University, Ottawa, Ontario, K1S 5B6, Canada*

## Abstract

The design, manufacturing and testing of a prototype flapping-wing mechanism for a Bio-Inspired Micro Air Vehicle (BMAV) is described. The design process is guided by the following initial performance requirements and size parameters of the BMAV, which are set for a hypothetical surveillance mission: it shall hover in place, it shall record and transmit live video wirelessly and it shall have no dimension greater than 150mm in length. A mathematical model of the flapping wing kinematics is developed and coupled with a modified aerodynamics model to guide the design process through quantitative estimates of the forces, torques, work and power required in flapping-wing hovering flight. It is assumed that the wing oscillatory flapping is harmonic, which is observed in many flapping-wing vertebrates and invertebrates. The stroke plane is aligned with the horizontal plane in the current design. Also, the planform of the flapping-wing and its straight leading-edge enable precise rotation of the wing tip relative to the wing root. The wing resultant aerodynamic force, wing average lift coefficient, torque at the root of the wing and the total power required per flapping cycle are calculated. A prototype of the proposed wing and flapping mechanism is designed and constructed using commercial off-the-shelf components to validate the mathematical model. The design of the prototype wing is optimized to achieve an average lift coefficient of 1.8. The chosen wing skin material is polyurethane coated nylon fabric. The leading-edge spar was designed to permit the attachment of skins of various sizes. To achieve a relatively constant angle of attack of 23 degrees, a planetary gear train is designed and mounted between the wing's root rib and pivot point. Brushless motors have been chosen to power the flapping mechanism given their advantages over brushed motors. The flapping-wing mechanism has successfully been constructed, and its functionality has been validated. The current stage of the study focuses on testing its aerodynamic performance using an in-house designed and constructed BMAV test stand, which is described and discussed in this paper.

## 1.0 Introduction

BMAVs offer several advantages when compared to other Unmanned Aerial Systems (UASs). Given their subcompact size, they can navigate in environments that are inaccessible to other UASs, such as the dense foliage found in automated vertical farms, small shafts in underground mining and passageways partially blocked by debris; they can perform complex manoeuvres that are not possible with other aerial platforms; they are environmentally friendly; and possess the element of stealth [1]. Research in BMAVs is multidisciplinary by nature and depends on advances made in several fields including flapping wing aerodynamics, structures and materials, mechanisms, control engineering, electronics and system design. Flapping-wing aerodynamics

---

<sup>1</sup> MEng, Mechanical and Aerospace Engineering, Carleton University, Ottawa, ON, Canada

<sup>2</sup> BEng Student, Mechanical and Aerospace Engineering, Carleton University, Ottawa, ON, Canada

<sup>3</sup> Assistant Professor, Mechanical and Aerospace Engineering, Carleton University, Ottawa, ON, Canada

<sup>4</sup> Professor, Mechanical and Aerospace Engineering, Carleton University, Ottawa, ON, Canada

<sup>5</sup> Professor, Department of Biology, Carleton University, Ottawa, ON, Canada

research, which is a characteristic of all BMAVs, falls under the low Reynolds number unsteady aerodynamic regime [2]. The complexity of the flow around the flapping wing, which increases significantly when wing flexibility and other physical details are considered, renders the development of empirical aerodynamic models attractive for control and flight stabilities investigations [3]. Several examples of empirical aerodynamic models of flapping-wing exist in the literature as reviewed by Shyy et al. [4]. This paper presents the initial stages of building the infrastructure to investigate the development of semi-empirical aerodynamic models of flexible flapping wings.

## 2.0 Design, Calibration and Commissioning of The Test Stand

### 2.1 Design

A flapping-wing flight test stand was designed and constructed. The test stand prototype and schematics are shown in Figure 1. The flight test stand is divided into three main levels: the base plate, drag platform and lift platform that is seated on the drag platform.

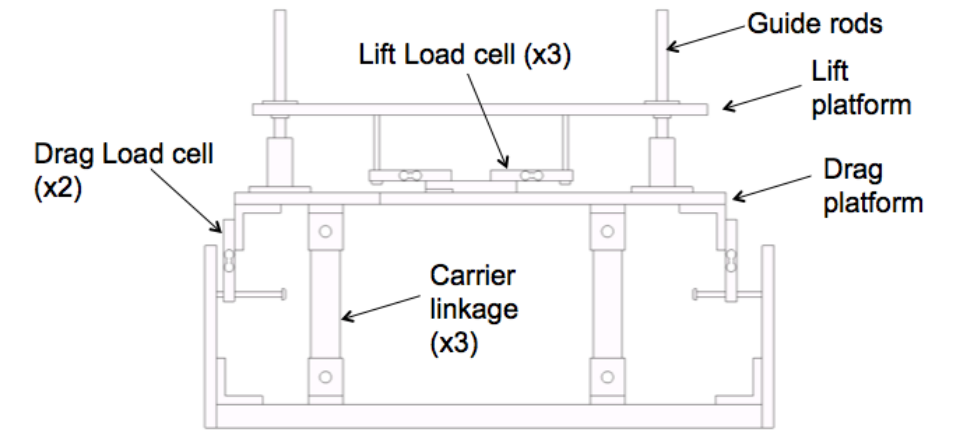


Figure 1: Schematics of Test Stand Prototype.

The two platforms are constrained in the lateral and longitudinal direction such that they move simultaneously with respect to the base plate. The lift platform is constrained in the vertical direction while the drag platform is constrained in the longitudinal direction. Three calibrated CZL616C 780g-load Micro Load Cells, which are elevated on the drag platform using an adapter plate, measure the lift forces of any mechanism mounted on the platform. The drag forces are then measured by restraining the longitudinal motion using calibrated load cells forward and aft of the test stand.

Three aluminum carrier linkages mounted on pinned joints are used to support the drag platform from the base plate. A flanged bushing and washer act as the interface between the linkage and the pin and between the linkage and the bracket faces. The bushing-washer configuration minimizes the static friction generated in the joint without the use of lubricants. The linkage when mounted perpendicularly transmits only vertical forces to counteract the moment caused by the drag on the wings during flapping. The lift and drag platforms were manufactured out of high-density polyethylene (HDPE) as it is easy to machine and readily available. Other components were made out of 6061 aluminum.

Possible sources of error in the measurements that stem from the design and construction of the test stand are: vibrations in the lift or drag platforms; friction in linkages; the carrier linkages not perpendicular to the ground causing errors in drag measurement; misalignment of the guide rods; and un-levelling of the lift platform due to drag moments leading to increased static friction, which causes errors in lift measurement.

## 2.2 Calibration and Commissioning

A data acquisition system and AxoScope software were used to collect data with a sampling rate of 1000Hz and low-pass filter of 0.01Hz. The CZL616C 780g-load Micro Load Cells (rated output of  $0.8 \pm 0.1$  mV/V) calibration was done using dead masses ranging from 5g to 50g on the centre of mass of the lift platform. The calibration result for the lift load cell is graphically presented in Figure 2.

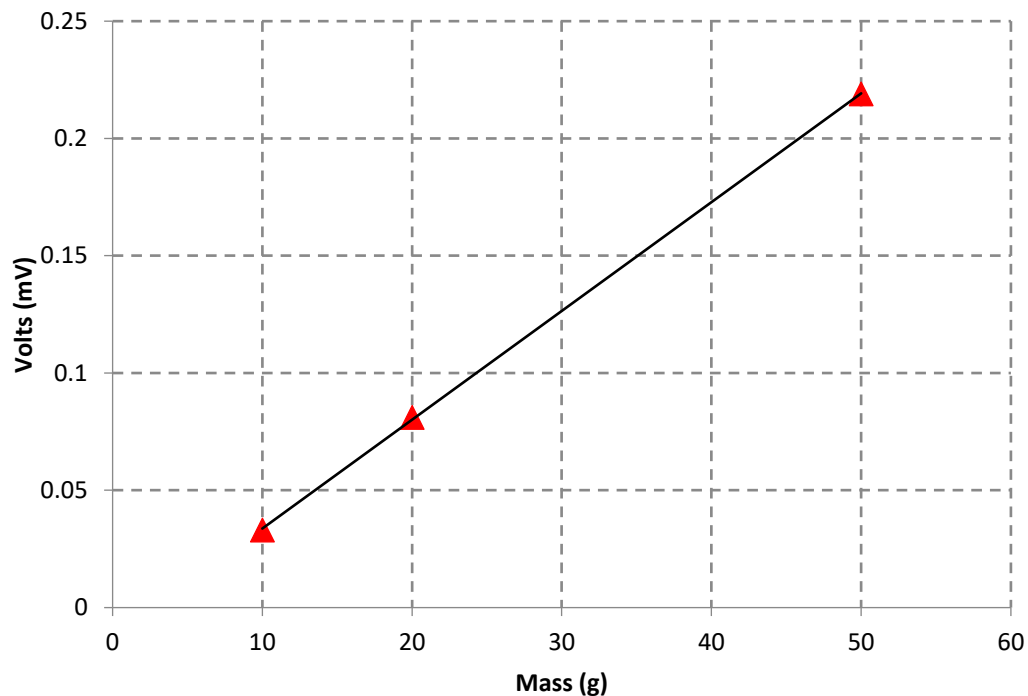


*Figure 2: Summarized Calibration Curve for Lift Load Cell.*

Pulley system was used to calibrate the drag fore-aft load cells in a way that there will be deflection on the load cell. Figure 3 and Figure 4 show the calibration curve for the drag aft and drag fore respectively.

The flight test stand was commissioned using airfoil lift testing in a 30cm×30cm wind tunnel. The NACA 0012 was chosen for this test as shown in Figure 5. Several runs were performed for angles of attack ranging from -10 degrees to 10 degrees. The runs for a fixed angle of attack were averaged to give the average lift force using the calibration curve in Figure 2. The average lift coefficient was then extracted from the quasi-steady aerodynamic lift equation [5] knowing the wind tunnel flow velocity and using sea-level air density. The wind tunnel was run at low airspeeds as to render compressibility effects negligible. The obtained measured lift coefficient for the airfoil was compared to the published NACA airfoil results as shown in Figure 6.

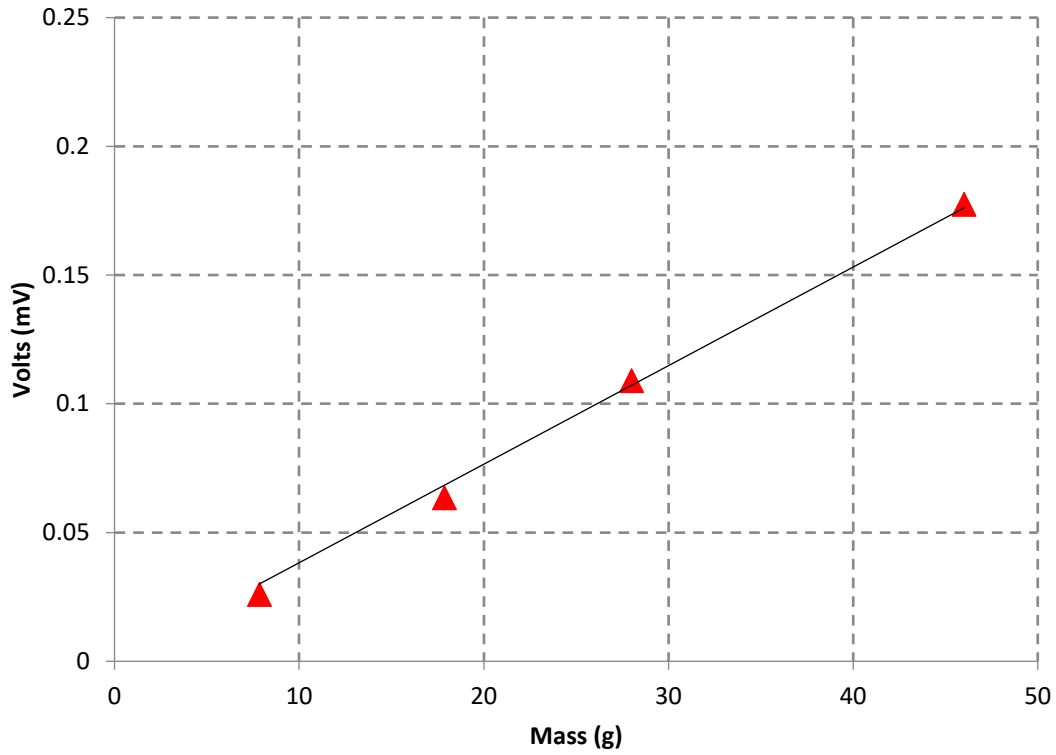


Figure 3: Drag/Aft Load Cell Calibration Curve.

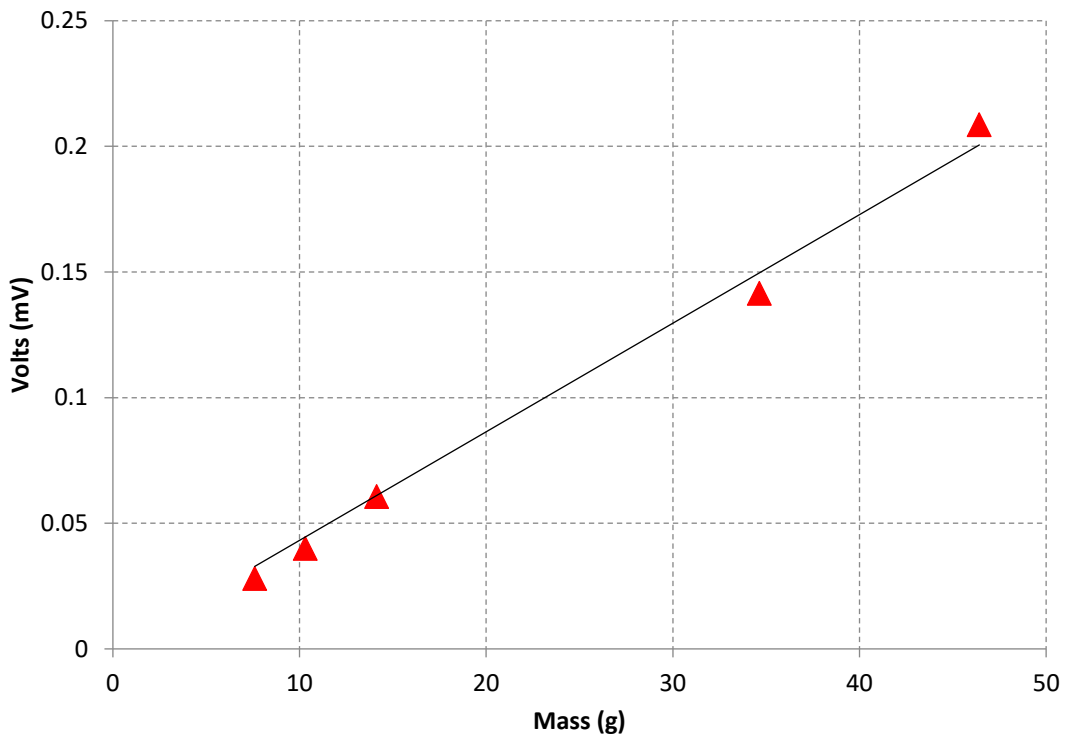


Figure 4: Drag/Fore Load Cell Calibration Curve.

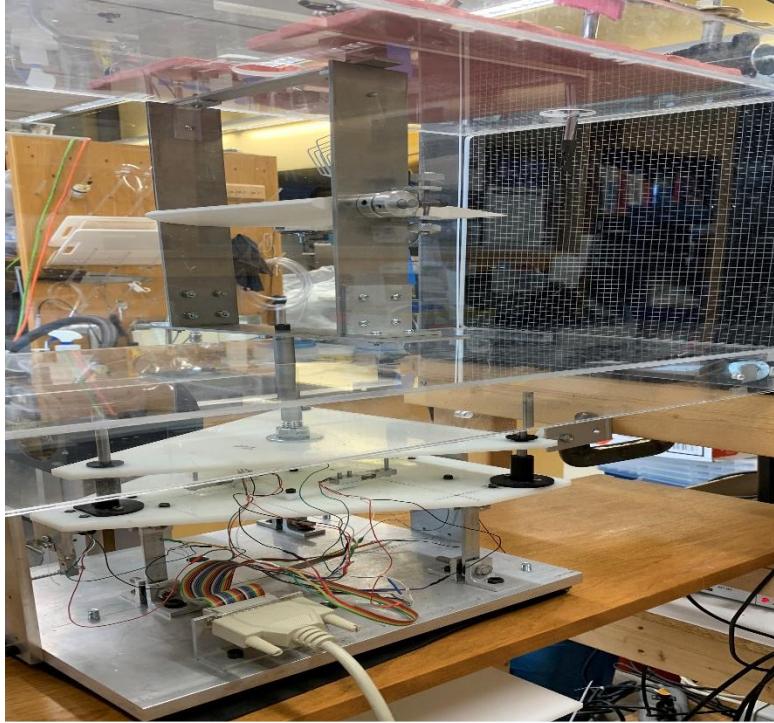


Figure 5: Commissioning of the test stand using NACA0012 airfoil.

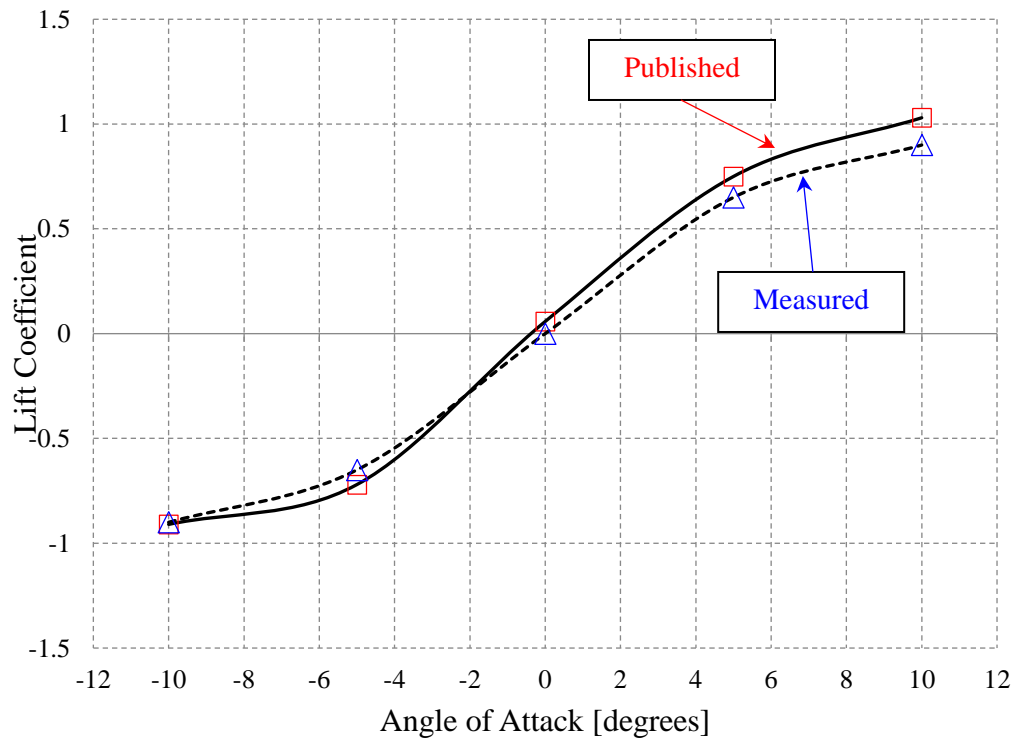


Figure 6: NACA0012 Measured vs Published Lift Coefficient.

### 3.0 Modelling of Wing Flapping Kinematics, Dynamics and Aerodynamics

An analytical model is constructed that will permit quantitative estimates of the forces, energy and power of a hovering flapping-wing flyer. Natural flapping-wing flyers accomplish flight through the oscillation of their wings. The kinematics and the structural deformations of the flapping wings are now known to produce aerodynamic force augmentation mechanisms [2] that are still being researched and investigated. Understanding those mechanisms is essential for developing aerodynamic models of flapping-wing flyers that can be used to design efficient flight control strategies for BMAVs.

#### 3.1 Kinematics

The angular motion of the lateral wing axis is approximately sinusoidal in many flapping-wing vertebrates and invertebrates. Deviations from perfectly harmonic oscillations tend to increase the forces acting on the wing, and thereby increase the bending loads on the wing structure. Such deviations pose challenges to representing the instantaneous position of the wing's lateral axis with respect to time. For this study, it is assumed the wing's angular oscillations can be represented using a harmonic function. The motion of the lateral axis is generally confined to the stroke plane. For most natural flapping-wing flyers, this stroke plane is tilted slightly by the angle  $\beta$ , such the wing tips trace an elongated figure eight path in the air. This study will assume, however, that the stroke plane is aligned with the horizontal plane.

Applying the method described by Weis-Fogh [6], the instantaneous angular position of the lateral wing axis can then be written as,

$$\gamma = \frac{1}{2}\pi + \frac{1}{2}\phi \sin\left(\frac{2\pi t}{t_o} - \frac{\pi}{2}\right) \quad (1)$$

where  $\phi$  is the stroke excursion angle, equal to two times the stroke amplitude,  $t_o$  is the period of one complete stroke,  $t$  is the instantaneous time, and  $n$  is the flapping frequency; such that,

$$t_o = \frac{1}{n} \quad (2)$$

Therefore, the angular velocity can be written as,

$$\dot{\gamma} = \frac{d\gamma}{dt} = \pi\phi n \cos\left(2\pi n t - \frac{\pi}{2}\right) \quad (3)$$

And similarly, the angular acceleration can be written as,

$$\ddot{\gamma} = \frac{d^2\gamma}{dt^2} = -2\phi\pi^2 n^2 \sin\left(2\pi n t - \frac{\pi}{2}\right) \quad (4)$$

Considering an individual spanwise wing element of width  $dR$ , whose center is located a distance  $r$  from the wing pivot, has a linear velocity of,

$$v_r = r\dot{\gamma} \quad (5)$$

### 3.2 Dynamics

Employing Eq. (4), we can express the inertial torque due to acceleration at any instant in time,

$$Q_I = I\ddot{\gamma} = -2I\phi\pi^2n^2\sin\left(2\pi nt - \frac{\pi}{2}\right) \quad (6)$$

where  $I$  is the moment of inertia of the wing about its pivot.

In order to calculate the total aerodynamic forces and torques, the local relative incoming wind velocity  $V_r$  at each wing element, as identified in Figure 7, must be determined. The magnitude and direction of  $V_r$  will be the vector sum of the linear velocity  $v_r$ , using Eq. (5), and the induced velocity of the wake immediately below the stroke plane,  $w$ .

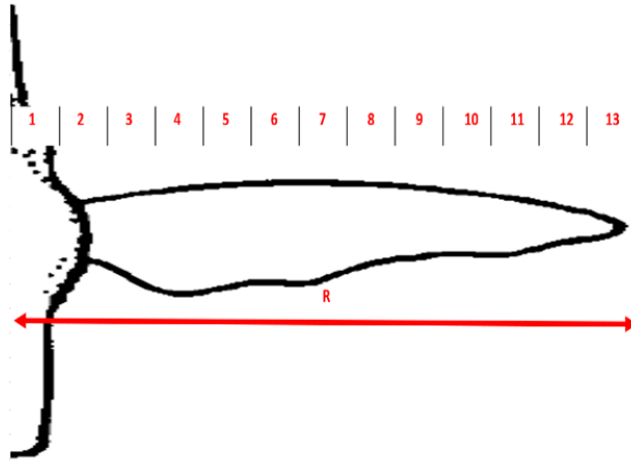


Figure 7: Wing Element Numbering (modified from [1]).

Actuator disc analogy is used to define the induced velocity,  $w$ . The effect of the actuator disc is to accelerate the incoming flow in the direction normal to the stroke plane. There is an assumption made that the induced flow velocity is uniform from root to tip and no whirling motion is created. When hovering, the momentum imparted by the actuator disc to the air must be equal to the body's weight,  $W$ . By the momentum theory for an ideal actuator disc, the induced wind velocity in the immediate wake [7] is,

$$w^2 = \frac{W}{2\pi\rho R^2} \quad (7)$$

where  $R$  is the disc radius that can be equated to the wing's length from root to tip.

The following simplifying assumptions are invoked to simplify the analysis. First, the induced wind velocity is assumed constant throughout the entire wing stroke cycle and without whirl. Second, the stroke excursion of each wing is a full  $180^\circ$  range of sweep. The justification provided by Weis-Fogh [6] for the use of such an analytical model for predicting flapping-wing performance under these assumptions is based on: the analysis remains conservative since no additional unsteady mechanisms are aiding lift generation, estimated effects brought on by non-uniformity

are relatively small and experimental measurements of the mean induced velocity in the immediate wake have strong agreement with predictions using ideal actuator momentum theory.

The resulting instantaneous resultant aerodynamic force  $F_r$  acting on each wing element can therefore be expressed as,

$$F_r = \frac{1}{2} \rho V_r^2 A_r (C_L^2 + C_D^2)^{\frac{1}{2}} \quad (8)$$

where  $A_r$  is the area of particular wing element,  $C_D$  is the coefficient of drag, and  $C_L$  is the coefficient of lift.

Figure 8 provides an illustration of the angles, velocities, and force components acting on any given wing-element during hover.

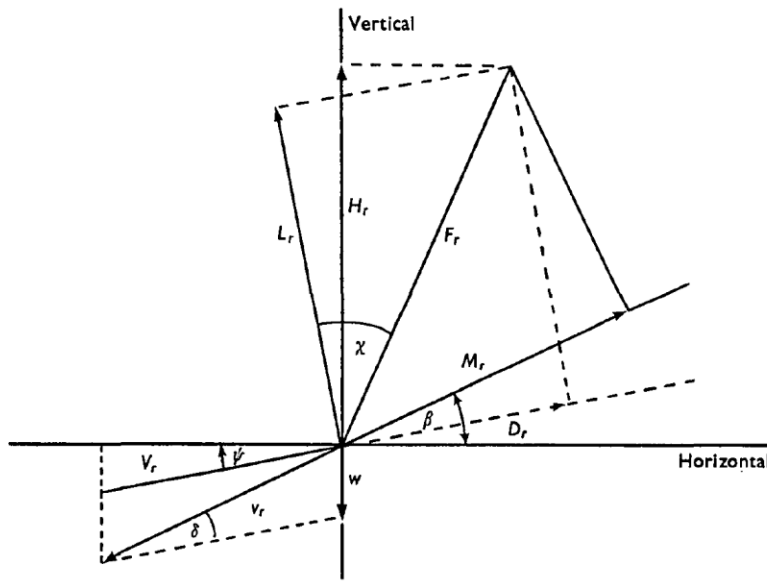


Figure 8: Angles, Velocity and Force Components [1].

By trigonometry, the law of cosines can be re-arranged to express the relative incoming wind velocity at any wing element,

$$V_r^2 = v_r^2 + w^2 - 2wv_r \sin\beta \quad (9)$$

where the angle  $\delta$  between  $V_r$  and  $v_r$  and the angle  $\psi$  between  $V_r$  and the horizontal axis are,

$$\sin\delta = \frac{w \cos\beta}{V_r} \quad (10)$$

$$\psi = \delta - \beta \quad (11)$$

Figure 8 also introduces the angle between the resultant aerodynamic force components of lift and drag labelled  $\chi$ , which can be represented by,

$$\frac{C_D}{C_L} = \tan\chi \quad (12)$$

We can now re-express the resultant aerodynamic force acting on wing element in terms of  $\chi$  as,

$$F_r = \frac{\frac{1}{2}\rho V_r^2 A_r C_L}{\cos\chi} \quad (13)$$

Resolving the resultant aerodynamic force into the  $H_r$  and the  $M_r$  components shown in Figure 8,

$$H_r = \frac{\frac{1}{2}\rho V_r^2 A_r C_L \cos(\chi + \psi)}{\cos\chi} \quad (14)$$

$$M_r = \frac{\frac{1}{2}\rho V_r^2 A_r C_L \sin(\chi + \psi + \beta)}{\cos\chi} \quad (15)$$

Defining the dynamic pressure  $p_r$  acting on any given wing-element as,

$$p_r = \frac{1}{2}\rho V_r^2 A_r \quad (16)$$

The aerodynamic torque opposing the flapping motion of any given wing element is then,

$$Q_{A,r} = \frac{r p_r C_L \sin(\chi + \psi + \beta)}{\cos\chi} \quad (17)$$

### 3.3 Average Coefficient of Lift

Starting from the procedure originally proposed Weis-Fogh [6], the modelled wing is divided into thirteen equally long spanwise sections that were shown in Fig. 7. Each wing section is identified by a station index subscript  $i$ , where  $i = 1$  to  $13$ . The area of each wing section and the distance from the wing pivot to section center were calculated using a CAD software. Each quarter of the whole wing stroke period is divided into ten time-equidistant points, identified by a time index subscript  $j = 1$  to  $10$ . Figure 9 shows a plot of the calculated dynamic pressure index during the second half of the downstroke.

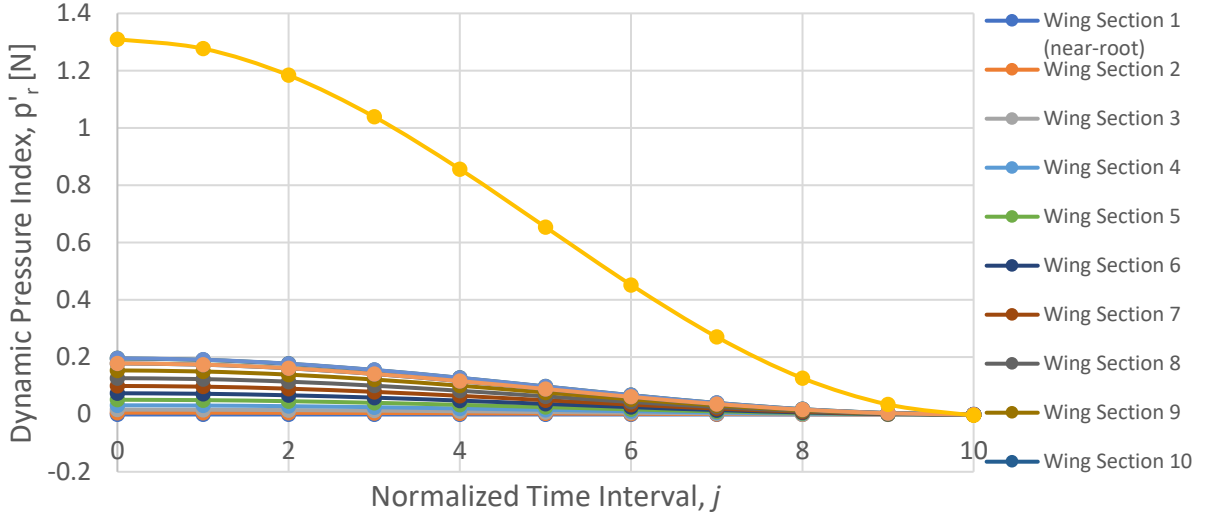


Figure 9: Vertical Dynamic Pressure Index over Quarter Cycle.

Finding the area below the summed curve and dividing by the number of time intervals results in an average value for the dynamic pressure index. In order for the flapping-wing to successfully hover, the weight of the platform must equal the average dynamic pressure index, multiplied by the average coefficient of lift  $\overline{C_L}$  over the quarter-period. Therefore, the average coefficient of lift can be expressed as,

$$\overline{C_L} = \frac{W}{\frac{\sum_{j=1}^{10} \sum_{i=1}^{13} p'_{i,j}}{10}} \quad (18)$$

In comparison to the measured average coefficient of lift for natural flapping-wing flyers, Weis-Fogh [1] concludes that this method of predicting  $\overline{C_L}$  is a good approximation. Weis-Fogh [6] notes that if the average coefficient of lift is found to be greater than what is achievable by the selected wing profile shape and Reynolds number, then this method of predicting the resultant aerodynamic forces and total power would no longer be valid. As obtained by Weis-Fogh [6], a reasonable  $C_L$  and  $C_L/C_D$ , as obtained from measurements on hummingbirds is 1.8 and 6, respectively.

#### 4.0 Design of The Flapping Wing and The Flapping Mechanism Demonstrator

In order validate the mathematical model presented in Section 3, a demonstration prototype of the proposed wing and flapping mechanism are designed and constructed. The details of the design of major sub-systems and overall assembly are presented.

##### 4.1 Baseline Parameters

In this study, the following requirements are established for a hypothetical surveillance application of the MAV, it shall: hover in place, record and transmit live video wirelessly and have no dimension greater than 150 mm in length.

To establish a baseline mass for the overall vehicle, the largest permissible wing area is considered given the limiting envelope dimension. This area would be the area of a circle of diameter  $d$ , where  $d = 150 \text{ mm}$ . Thus, the wing area  $S$  is given by,

$$S = \frac{\pi d^2}{4} = 17,671.5 \text{ mm}^2 \quad (19)$$

Applying the geometry scaling relations developed by Norberg [8] for *Birds, all*, the maximum vehicle mass attainable with a circular wing planform is,

$$m = \left( \frac{S}{0.69} \right)^{\frac{1}{1.04}} \sim 47 \text{ g} \quad (20)$$

Therefore, a baseline target mass of 47 g for the hypothetical MAV is selected.

Davis et. al [9] conducted a study of theoretical MAVs for surveillance missions. Applying their same distribution of mass to sub-systems, an estimate of the available mass for each sub-system is obtained and shown in Table I.

*Table I Mass Distribution*

<b>Sub-System</b>	<b>% of Total Mass Allotment</b>	<b>Theo. Sub-System Mass [g]</b>
Flight Controller	4.1%	1.9
Payload	10.2%	4.8
Propulsion	73.5%	34.5
Wings	6.1%	2.9
Body	6.1%	2.9

Hummingbirds serve as a good analog to flapping-wing MAVs, given their size and ability to hover. Applying the scaling functions for wing dimensions from Norberg [8] for *Hummingbirds*, and assuming a baseline MAV mass of 47 g, the initial design parameters for the flapping-wing MAV shown in Table II are obtained.

*Table II Baseline MAV Parameters*

<b>Wing Span [m]</b>	<b>Wing Area (both wings) [m<sup>2</sup>]</b>	<b>Wing Loading [N/m<sup>2</sup>]</b>	<b>Aspect Ratio</b>	<b>Wingbeat Frequency [Hz]</b>
0.4430	0.02870	16.160	6.85	5.3

#### 4.2 Wing Area Distribution

The hummingbird's ability to finely control their wing twist is challenging to re-create. A wing planform and structure compatible with controlling twist and amplitude, while minimizing weight and complexity, has been conceptualized. The ideal wing planform for minimizing induced drag is one that creates an elliptical lift distribution. The lift distribution produced by an elliptical wing planform is approximately elliptical itself and serves as a good starting point. Figure 10 shows a

top-down view of the selected planform (i.e. combination of Areas A2 ‘orange’ and A3 ‘red’). The selected planform shape is created from a full ellipse (i.e. Areas A1 ‘yellow’ and A2 ‘orange’), whereby the area above the major-axis A1 has been redistributed below A2 and labelled A3. This modified-elliptical planform allows for wing area  $S$ , wing span  $b$ , and aspect ratio  $AR$  to be retained, from the bio-scaling predictions in Table II.

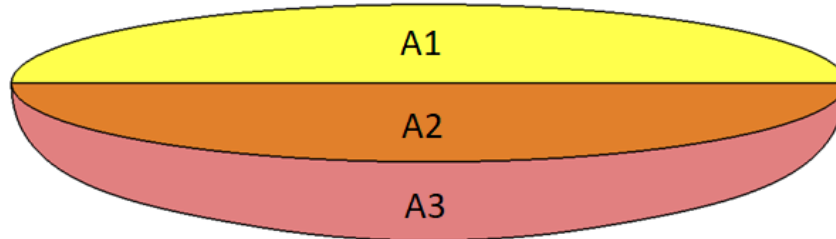


*Figure 10: Modified-Elliptical Planform (A<sub>2</sub> & A<sub>3</sub>).*

This method of applying geometric scaling relations allows for a quick estimation of the MAV wing geometry and kinematics, which is used as the starting point for further optimization.

#### 4.3 Wing Geometry Optimization

The optimal wing geometry that will support hovering of given flapping-wing mass and minimize power required is assumed to lie between the wing spans and areas predicted by Eq. (19) and the predictions by bio-scaling functions summarized in Table II. Employing the mathematical model presented above, the wing geometry is iterated upon in order to reduce power requirements while still maintaining a  $C_L$  below the 1.8 threshold. The model calculates the average coefficient of lift, at the provided wing span and section areas. The initial conditions use the largest value of wing span that was predicted in Table II. The wing span is decreased incrementally, while the aspect ratio is held constant. The iterations continue until the model converges on the target average coefficient of lift,  $\overline{C_L} = 1.8$ . Table III summarizes the optimized wing dimensions following several iterations of the model and shows the required average coefficient of lift. The final optimized geometry has a required average coefficient of lift of 1.7. Additional iterations could be made to converge the coefficient of lift closer to 1.8; however, a residual of 0.1 is sufficient in the context of this investigation.

*Table III Wing Geometry Optimization*

Wing Span [m]	0.325
Wing Area (both wings) [m <sup>2</sup> ]	0.01602
Wing-length, R [m]	0.133
Wing Moment of Inertia (1x) [kg-m <sup>2</sup> ]	0.0000621
"Natural Frequency", f <sub>w</sub> [Hz]	20.9
Average Coefficient of Lift, C <sub>L_bar</sub>	1.7
<b>Areas of Wing Sections</b>	
Area 1, Ar,1 [m <sup>2</sup> ]	0
Area 2, Ar,2 [m <sup>2</sup> ]	0.005999806
Area 3, Ar,3 [m <sup>2</sup> ]	0.000601833
Area 4, Ar,4 [m <sup>2</sup> ]	0.00057109
Area 5, Ar,5 [m <sup>2</sup> ]	0.000568183
Area 6, Ar,6 [m <sup>2</sup> ]	0.000548998
Area 7, Ar,7 [m <sup>2</sup> ]	0.000527856
Area 8, Ar,8 [m <sup>2</sup> ]	0.00050379
Area 9, Ar,9 [m <sup>2</sup> ]	0.000475324
Area 10, Ar,10 [m <sup>2</sup> ]	0.000440161
Area 11, Ar,11 [m <sup>2</sup> ]	0.00039444
Area 12, Ar,12 [m <sup>2</sup> ]	0.000329928
Area 13, Ar,13 [m <sup>2</sup> ]	0.000201787

#### 4.3 Wing Skin Material

Selecting a material for the construction of the wing skin posed a surprisingly difficult challenge. The functional requirements are for it to be lightweight, pliable, and strong enough to carry the wing loading. Several composite materials were considered, which typically consist of a fabric substrate and bonding resin. Consideration was also given to polyvinyl chloride (PVC) films on the order of 0.25 to 0.5 mm thick. Table IV lists some of the materials considered and their respective area densities.

*Table IV Wing Skin Materials*

<b>Material</b>	<b>Fabric Density [g/m<sup>2</sup>]</b>
Carbon Fiber Tissue + Epoxy	20
Polyvinyl Chloride (PVC) "20 Gauge"	660
Ripstop Nylon Sailcloth	32
Polyurethane Nylon Fabric	48

Ultimately, the chosen wing skin material was a polyurethane (PU) coated nylon fabric at 48 g/m<sup>2</sup>. This material is often used in the construction of lightweight sails, kites, and flags. The material has attractive characteristics, and most notably adapts well to the kinematics of the wing. This material is also relatively inexpensive, easy to assemble, and readily available.

#### 4.4 Wing Structure

The selected planform is also chosen for its straight leading-edge, which enables precise rotation of the wing tip relative to the wing root and ease of attachment for the wing skin. Figure 11 shows the simple and lightweight wing structure, consisting of leading-edge spar.

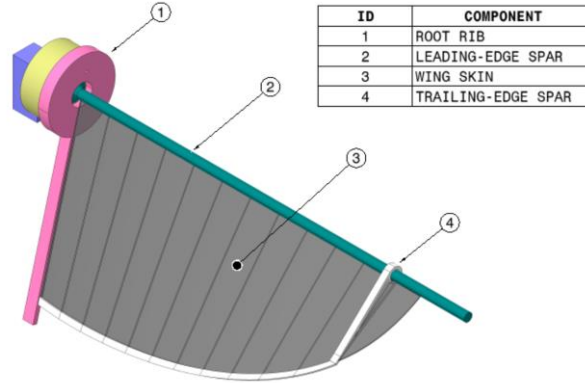


Figure 11: Wing Structure.

The leading-edge spar was designed to permit the attachment of skins of various sizes. The spar will accept wing lengths up to 192 mm and root chords up to 90 mm in length. The manufacturing method chosen for the spar was a process known as stereolithography (SLA) using Somos NeXt resin. The spar diameter was sized based on the critical loading case at the maximum wing length. Table V summarizes the results of mathematically modelling the resultant aerodynamic forces  $F_{r,i}$  and its resolved components in the vertical direction  $H_{r,i}$  acting on each of the wing sections. The values for  $F_{r,i}$  at each section are the larger of the two force components and were selected as the design limiting case for the spar.

Table V Resultant Aerodynamic Forces and Components

		Resultant Aerodynamic Forces, $F_{r,i}$ [N] Eq. 13	Hovering Force Components, $H_{r,i}$ [N] Eq. 14	Station Centre, $r_i$ [m]
Station Index, $i$	1	0.0000	0.0000	0.0074
	2	0.0089	0.0070	0.0222
	3	0.0209	0.0185	0.0370
	4	0.0379	0.0350	0.0517
	5	0.0595	0.0561	0.0665
	6	0.0849	0.0810	0.0813
	7	0.1134	0.1090	0.0961
	8	0.1436	0.1387	0.1109
	9	0.1737	0.1683	0.1257
	10	0.2007	0.1951	0.1405
	11	0.2196	0.2139	0.1552
	12	0.2201	0.2146	0.1700
	13	0.2000	0.1953	0.1848

#### 4.4 Flapping Mechanism Planetary Gear Train

To achieve a relatively constant angle of attack of  $23^\circ$ , a planetary gear train is designed and mounted between the wing's root rib and pivot point. Using a wing length of  $R = 192 \text{ mm}$  and wingbeat frequency  $n = 15 \text{ Hz}$ , the angle  $\psi$  of the relative incoming wind velocity is determined for each wing section at each time index  $j$  over a one-quarter period. The desired average angle of attack  $\bar{\alpha}$  over the whole wing stroke period is  $23^\circ$ . Therefore, the desired average angle of attack at each wing station  $\bar{\alpha}_i = 23^\circ$ . This  $\bar{\alpha}_i$  can be expressed as,

$$\bar{\alpha}_i = \frac{\sum_{j=0}^{40} (\theta_{w,i,j} - \psi_{r,i})}{41} \quad (21)$$

Therefore, at each wing station  $i$ , the required geometric angle of attack of the wing relative to the horizontal  $\theta_{w,i}$  can be solved by,

$$\theta_{w,i} = \frac{41\bar{\alpha}_i + \sum_{j=0}^{40} \psi_{i,j}}{41} \quad (22)$$

Omitting the region of the wing near the wing pivot where no skin is applied, the required geometric angle of attack at the wing root  $\theta_{w,root} = 40^\circ$  and near the wing tip  $\theta_{w,tip} = 56^\circ$ . Therefore, the relative twist between these locations is  $16^\circ$ , which corresponds to a train ratio  $e = 1.4$ .

The sun gear's rotation is held stationary by attaching it directly to the wing pivot. The planet carrier, which also acts as the thrust bearing, is driven by the motion of the root rib that moves according to the forces acting against the wing skin at the root. The drive ring gear is attached to the leading-edge spar, which is fixed to the trailing-edge spar at the wing tip. Figure 12 shows the overall assembly and lists the number of teeth on each respective gear, which results in an approximate train ratio of  $e = 1.5$ .

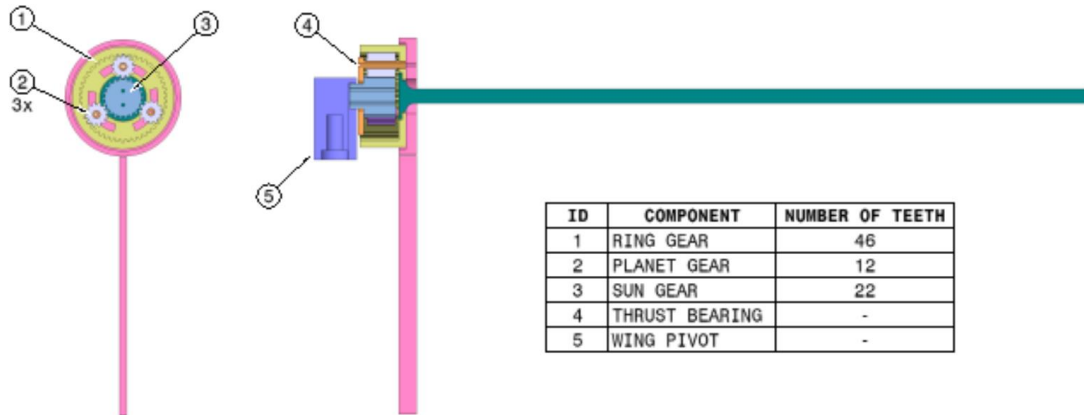


Figure 12: Planetary Gear Train.

#### 4.5 Power Requirement

To find the power required to drive the flapping-wing about its pivot point, the mathematical model developed in Section 3 is utilized. The maximum power required will be determined based on the largest wing length  $R$  that can be accommodated by the leading-edge spar. The maximum wing length parameters are listed in Table VI.

Table VI Maximum Wing Length Parameters

Maximum Length Wing	
Mass Flight Controller [kg]	0.0019
Mass Payload [kg]	0.0048
Mass Propulsion [kg]	0.0345
Mass Wings (2x) [kg]	0.0362
Mass Body [kg]	0.0029
Totals Mass [kg]:	0.0803
Wing Span [m]	0.443
Wing Area (both wings) [m <sup>2</sup> ]	0.02870
Wing-length, R [m]	0.192
Wing Moment of Inertia (1x) [kg-m <sup>2</sup> ]	0.0001140
"Natural Frequency", $f_w$ [Hz]	14.7
Average Coefficient of Lift, $C_{L\_bar}$	1.1

At each time index  $j$ , the inertial torque is determined by Eq. (6) and the aerodynamic torque by Eq. (17). The total torque at any given instant is the summation of these two values. Figure 13 shows the torque versus the instantaneous position of the wing across the entire wing-stroke period. The area under the curves represents the work done by torque.

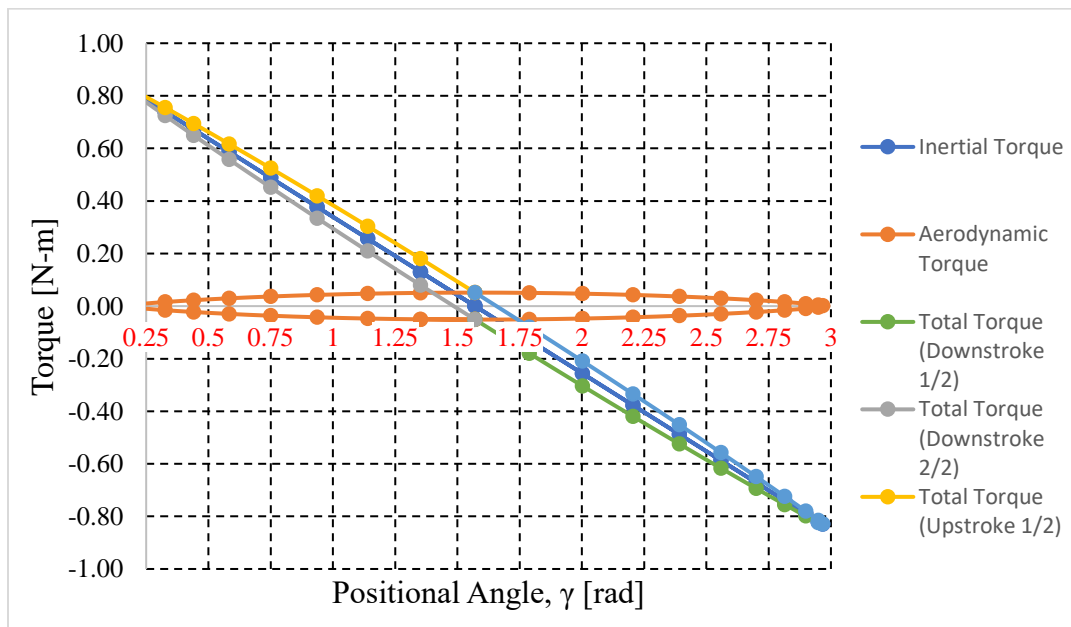


Figure 13: Work of Total Torque.

As evident in Fig. 13, the maximum total torque of  $Q_{T,max} = 0.828 \text{ N}\cdot\text{m}$  occurs at the moment of stroke-reversal, or  $\gamma = 0.1745 \text{ rad}$  and  $2.9671 \text{ rad}$ . The majority of the total torque at this instant is due to inertial acceleration, with virtually zero contribution by aerodynamic torque. Thus, the power expended to overcome the aerodynamic forces at a flapping frequency is,

$$P_A = nW_A \quad (23)$$

where  $n$  is the flapping frequency.

The total power to overcome the aerodynamic and inertial forces during the upstroke and downstroke is then found by,

$$P_T = n \int_{\gamma_{min}}^{\gamma_{max}} (Q_A + Q_I) d\gamma + n \int_{\gamma_{max}}^{\gamma_{min}} (Q_A + Q_I) d\gamma \quad (24)$$

Using Eqs. (23) and (24), the total power required at the wing pivot is determined. The maximum total power  $P_{T,max} = 0.0952 \text{ W}$ , occurring at the one-quarter point into each half-stroke, which is  $\gamma = 0.5835 \text{ rad}$  and  $2.5581 \text{ rad}$ .

#### 4.6 Power Transmission

Once the required torque at the wing pivot was determined, a suitable mechanism for transmitting power to the wing was conceptualized. One requirement of the mechanism was to have independent control of each wing, such that variations in power between wings could produce moments about the vehicle axes for control in-flight. A second was to be lightweight, which results from minimal components and high power-density of the prime mover. Lastly, the power transmission was to be compatible with readily available COTS components to minimize cost and increase standardization. The design of the power transmission mechanism was arrived at after consideration of several types of prime movers, with a decision made to use an electric rotary motor. Thus, an additional requirement imposed on the mechanism was to also convert this rotary motion to oscillatory motion at the wing pivot. The well-known device called a *Scotch-Yoke* was selected for this conversion of motion types. Figure 14 illustrates its operation,

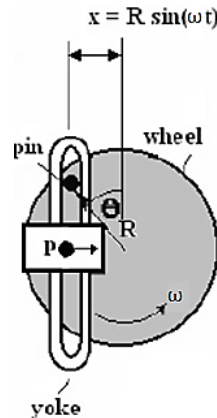


Figure 14: Scotch-Yoke.

As the wheel rotates the attached pin moves around the circumference. The pin is positioned in the hollow of the yoke, such that the yoke's position on the horizontal axis is determined by the location of the pin. An added benefit of the Scotch-Yoke is that the resulting velocity of point  $P$  follows a sinusoidal output based on a constant rotation input velocity to the wheel. This creates an ideal scenario for two reasons: 1) a motor can be optimized to operate at constant speed, and 2) the angular velocity of the flapping-wing is approximately sinusoidal. Figure 15 illustrates the chosen power transmission gear train. Gear 1 is the pinion that attaches to the motor output. Gear 2 is used to reduce RPM and increase output torque. Gear 3 is mounted on the same shaft axis as Gear 2, so both gears share the same RPM. Gear 4 further reduces RPM and increases torque, while also serving as the driving wheel of the scotch-yoke. Component 5 is the yoke, which is driven by the pin on Gear 4. Gear 5 is a rack that is fixed to move with the yoke. Gear 6 meshes with the rack as the two oscillate back-and-forth, with its output driving the wing pivot. The Guides are fixed to the body and provide support and alignment to the motion of the yoke.

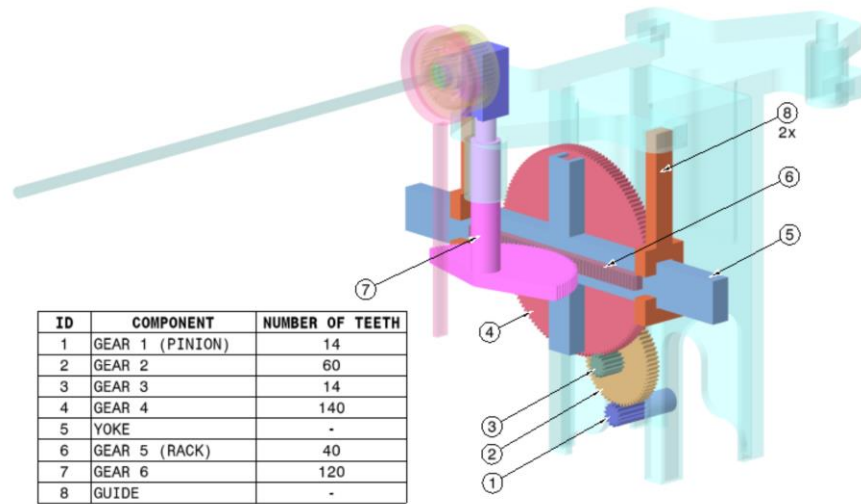


Figure 15: Power Transmission Gear Train.

#### 4.7 Motor Selection

For low-cost off-the-shelf electric motors, a range of direct current (DC) motors types were considered. The reason for opting for DC motors is to ensure compatibility with an envisioned portable power supply in the form of a battery. Other advantages of DC motors are that they allow for speed control, have an approximately linear speed-torque relationship, and offer high power density. There are two sub-classes of DC motors: brushed motors and brushless motors. Brushed motors have the advantages of simple control method, lower initial cost, and fewer electronic components. There are, however, some significant disadvantages of brushed motors such as: higher maintenance costs, reduced torque at high speed, restricted heat dissipation, and potential electric arcing at brush contacts. At a comparable operating torque rating, brushless motors have the advantages of higher efficiency, lower maintenance costs, reduced size, better heat dissipation, and higher power output. The trade-off is that brushless motors have a slightly higher initial cost and require the addition of an electronic speed controller (ESC), which adds weight and

complexity. In this flapping-wing drive application, brushless motors have been chosen given their advantages over brushed motors. The additional weight and complexity of implementing brushless motors is almost negligible, as the combined motor and ESC weight is still less than the weight of comparable brushed motor. The popularity of brushless motors in the radio control hobby community has brought about increasingly simple ESC solutions that are easy to integrate into miniature electronic applications.

Brushless motor manufacturers generally provide the following parameters in their motor specifications: velocity constant  $K_v$ , motor resistance  $R_m$ , no-load current  $I_o$ , and maximum allowable current  $I_{max}$ . Hendershot and Miller [11] offer several formulas to determine the useful RPM and torque output based on these parameters. With an available current  $I_{app}$  the resulting RPM, output torque, and motor efficiency can be calculated using the following,

$$RPM = K_v(I_{app} - I_o) \quad (25)$$

$$Q = K_q(I_{app} - I_o) \quad (26)$$

$$\eta = \frac{(V_{app} - I_{app} * R_m)(I_{app} - I_o)}{(V_{app} * I_{app})} \quad (27)$$

where,

$$K_q = \frac{60}{(2\pi K_v)} \quad (28)$$

A comprehensive market survey of low-cost readily available brushless DC motors was conducted to source a suitable driver of the maximum length flapping wing that can be accommodated on the demonstration rig. The chosen motor is the *Multistar Viking 2208/2600KV* manufactured by Turnigy Power Systems, as shown in Figure 16, along with its specifications.



Parameter	Value
Shaft Diameter, $d_{motor}$ [m]	0.003
Mass, $m$ [g]	25.3
Velocity Constant, $K_v$ [RPM/V]	2600
Motor resistance, $R_m$ [Ohm]	0.032
No load current, $I_o$ [A]	2.368
Max. Current, $I_{max}$ [A]	39.1
Supply Voltage, $V$ [V]	14.8

Figure 16: *Multistar Viking 2208/2600KV*.

The output shaft of the motor is attached to the axis of rotation of Gear 1 in the power transmission gear train. As determined previously, the constant rotational speed required at Gear 1 is  $\omega_1 = 51,013 \text{ RPM}$ . The time-varying operating torque required at Gear 1 is converted to an equivalent torque root-mean-square  $Q_{RMS,1}$  to permit comparison with the motors stall torque  $Q_{stall,motor}$ .

$$Q_{RMS,1} = \frac{\sum_{j=0}^{40}(Q_{1,j}^2 \Delta t_j)}{\sum_{j=0}^{40}(\Delta t_j)} = 0.0497 \text{ Nm} \quad (29)$$

and,

$$Q_{stall,motor} = K_q(I_{max} - I_o) = 0.1349 \text{ Nm} \quad (30)$$

A safety factor of 30% is applied to  $Q_{RMS,1}$  to accommodate for friction and winding losses in the operational torque requirement of Gear 1,

$$Q_{operation,1} = 1.3 * Q_{RMS,1} = 0.0646 \text{ Nm} \quad (31)$$

Comparing the operational torque requirement of *Gear 1* with the motor stalling torque, we find there is sufficient overhead in the available torque for this motor to drive the flapping wing.

$$Q_{stall,motor} > Q_{operation,1} \quad (32)$$

#### 4.8 Electronic Speed Controller (ESC)

An electronic speed controller (ESC) is required due to the choice of implementing brushless motors. The ESC must be rated at a sufficient current to tolerate the current drawn by the motors while under load. Hendershot and Miller [11], provide this relation to estimate the current drawn,

$$I_{load} = \frac{Q_{operation,1}}{K_q} \sim 17.6 \text{ A} \quad (33)$$

Researching the market for a lightweight, multi-motor ESC capable of supplying at least 17.6 A of continuous current per motor resulted in a product manufactured by the company HobbyWing. The company produces the *XRotor Micro 40A 4in1 ESC*, with the specifications provided in Fig. 17.

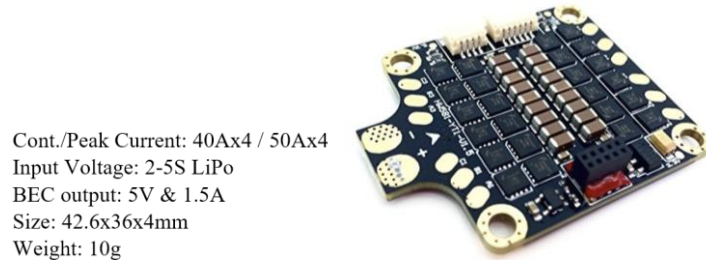


Figure 17: XRotor Micro 40A 4in1 ESC [12].

#### 4.9 Flight Controller

A flight controller is implemented in this study for several reasons: 1) to provide control I/O to motors, 2) to enable wireless connectivity, 3) to record and transmit video stream. The most

computationally intensive task is the wireless transmission of live video from the vehicle. It is for this reason that a controller with a minimum processor speed of 1 GHz was deemed necessary.

Reviewing common single-board computers revealed several candidates to serve as the flight controller. Ultimately the *Raspberry Pi Zero W* was chosen for its fast processor, integrated wireless connectivity, low weight, and established community of users. Figure 18, shows the specifications and illustrates the architecture of the board.

Connectivity:  
802.11 b/g/n wireless LAN  
Bluetooth 4.1  
Bluetooth Low Energy (BLE)  
Mini HDMI and USB On-The-Go ports  
Micro USB power  
HAT-compatible 40-pin header  
Composite video and reset headers  
CSI camera connector

Processor:  
1GHz, single-core CPU

Memory:  
512MB RAM

Product Dimensions:  
66.0mm x 30.5mm x 5.0mm

Product Weight:  
9.3g



Figure 18: *Raspberry Pi Zero W* [13].

#### 4.10 Payload

To meet the requirements of the hypothetical surveillance mission established at the outset of this study, an electro-optical (EO) camera was implemented. The camera had to only be capable of delivering a wireless video stream and be as lightweight as possible. A suitable off-the-shelf camera that is compatible with the *Raspberry Pi* was found through an online distributor. Figure 19 shows the camera module and lists its specifications,



Connection: via the CSI bus  
Resolution: 5 megapixels  
Dimensions: 8.6mm x 8.6mm x 5.2mm  
Lens Diameter: 6.9mm  
Cable Length: 52mm  
Weight: 1.1g

Figure 19: *Raspberry Pi Zero EO Camera* [14].

#### 4.11 System Diagram

In this section a systems diagram is presented to show the overall electrical layout. The brushless motors are soldered to the ESC at inputs *M1* and *M3*. A suitable battery has been sourced and connected to the ESC. The battery is a lithium polymer composition with 4S 2,000 mAh 45C rating. The ESC supplies 5V power to the flight controller, via its built-in battery eliminator circuit (BEC). There are two signal wires connected to the flight controller at GPIO 13 and GPIO 19,

which send pulse-width modulation (PWM) signals to the ESC for control of motor 1 and 3, respectively. A pushwheel switch is also connected via GPIO to the flight controller, to allow the operator to vary the speed of the brushless motors. Based on position selection, 0 representing off and 7 representing maximum RPM, the motors can be sped up or slowed down incrementally. Lastly, the EO camera payload is connected to the flight controller via the CSI bus.

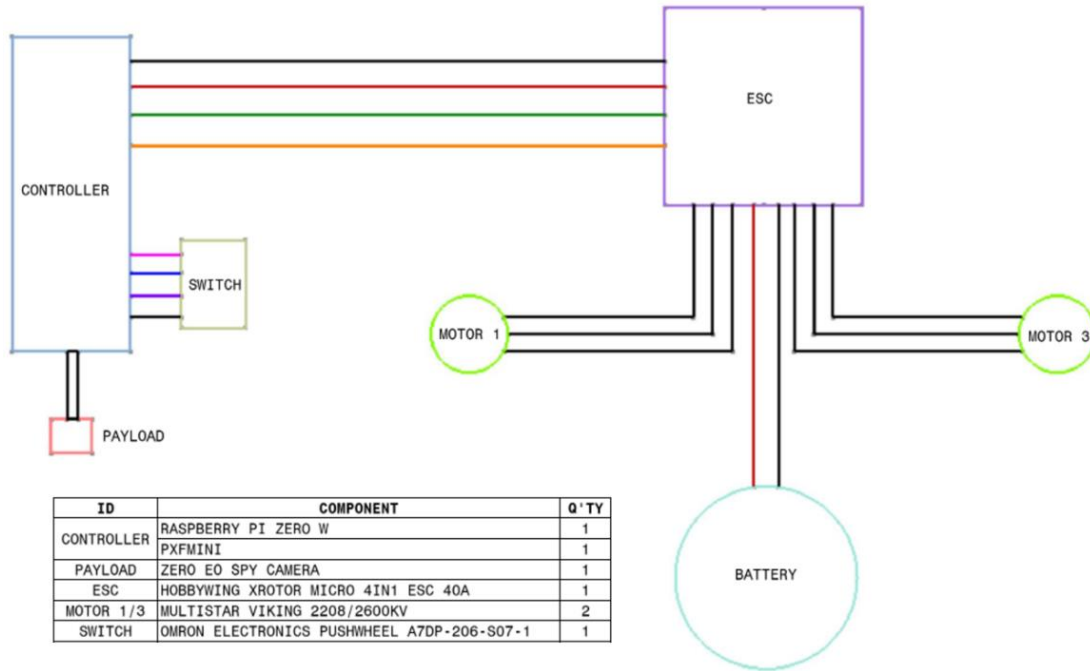


Figure 20: Systems diagram.

The wiring shown in Figure 20 has been tested and control of the brushless motor speed has been successfully achieved using the thumbwheel switch.

## 5.0 Future Work

Future work will focus on improving and digitizing the data acquisition system, addressing the misalignments of the test platform to improve the aerodynamic force measurements and securing the flapping mechanism with the wings attached to the platform to measure the flapping-wing generated aerodynamic forces.

## References

- [1] T. A. Ward, M. Rezaadad, C. J. Fearday and R. Viyapuri, "A Review of Biomimetic Air Vehicle," *International Journal of Micro Air Vehicles*, vol. 7, pp. 375-394, 2015.
- [2] D. D. Chin and D. Lentink, "Flapping wing aerodynamics: from insects to vertebrates," *Journal of Experimental Biology*, vol. 219, no. 7, pp. 920-932, 2016.
- [3] W. Shyy, H. Aono, S. K. Chimakurthi, P. Trizila, C.-K. Kang, C. Cesnik and H. Liu, "Recent progress in flapping wing aerodynamics and aeroelasticity," *Progress in Aerospace Sciences*, vol. 46, no. 7, pp. 284-327, 2010.
- [4] W. Shyy, C.-k. Kang, P. Chirarattananon, S. Ravi and H. Liu, "Aerodynamics, sensing and control of insect-scale flapping-wing flight," *Proceedings of the Royal Society of London A: Mathematical, Physical and Engineering Sciences*, vol. 472, no. 2186, 2016.
- [5] J. D. Anderson, *Fundamentals of Aerodynamics*, McGraw-Hill Education, 2016.
- [6] T. Weis-Fogh, "Energetics of Hovering Flight in Hummingbirds and in *Drosophila*," *J. Exp. Biol.*, vol. 56, no. 1, pp. 79–104, 1972.
- [7] W. Johnson, *Rotocraft Aeromechanics*. Cambridge University Press, 2013.
- [8] U. M. Norberg, *Vertebrate flight: mechanisms, physiology, morphology, ecology and evolution*, vol. 27. 1990.
- [9] W. R. Davis, B. B. Kosicki, D. M. Boroson, and D. F. Kostishack, "Micro Air Vehicles for Optical Surveillance," vol. 9, no. 2, pp. 197–214, 1996.
- [10] *McGraw-Hill encyclopedia of science & technology*, 10th ed. New York: McGraw-Hill, 2007.
- [11] J. R. Hendershot and T. J. E. Miller, *Design of Brushless PM motors*. Clarendon Press, 1994.
- [12] "XRotor Micro 40A 4in1 BLHeli-S DShot600\_Drone Systems\_HOBBYWING," 2017. [Online]. Available: <http://www.hobbywing.com/goods.php?id=588>. [Accessed: 19-Apr-2018].
- [13] Raspberry Pi Foundation, "Raspberry Pi Zero W," *Raspberrypi.Org*, 2017. [Online]. Available: <https://www.raspberrypi.org/products/raspberry-pi-zero-w/>. [Accessed: 19-Apr-2018].
- [14] "Raspberry Pi Spy Camera," 2017 [Online]. Available: <https://www.adafruit.com/product/3508>. [Accessed: 19-Apr-2018].